

Cite this: *J. Mater. Chem. A*, 2013, **1**, 4754

One-pot synthesis of a mesoporous NiCo₂O₄ nanoplatelet and graphene hybrid and its oxygen reduction and evolution activities as an efficient bi-functional electrocatalyst†

Dong Un Lee, Bae Jung Kim and Zhongwei Chen*

Mesoporous NiCo₂O₄ nanoplatelets and graphene sheets (NiCo₂O₄-G) are combined as a hybrid material via a one-pot synthesis process to demonstrate excellent bi-functional catalytic activity towards both the oxygen reduction reaction (ORR) and oxygen evolution reaction (OER). Physical characterizations have confirmed the formation of NiCo₂O₄ nanoplatelets created by selective adsorption of PVP onto specific crystal orientations, which provides spatial confinement for an anisotropic growth into 2-dimensional nanostructures. In addition, the decomposition of surface adsorbed PVP during the calcination process creates uniformly distributed meso-sized pores in the NiCo₂O₄ nanoplatelets. The beneficial hybrid and PVP effects are investigated via half-cell testing with NiCo₂O₄-G in comparison to graphene-free NiCo₂O₄ and PVP-free NiCo₂O₄-G, respectively, where much lower activation energy and higher current densities are observed with the mesoporous NiCo₂O₄-G hybrid for both ORR and OER. Furthermore, the positive impact of Ni incorporation was exclusively demonstrated, whereby NiCo₂O₄-G outperformed Co₃O₄-G in terms of onset potential and current densities for both ORR and OER. This is attributed to the increased electrical conductivity and the creation of new active sites with much lower activation energy due to the incorporation of Ni cations into the octahedral sites of the spinel crystal structure. This cost effective and highly efficient bi-functional catalyst is highly suitable for rechargeable metal-air battery technologies.

Received 6th December 2012
Accepted 7th February 2013

DOI: 10.1039/c3ta01402a

www.rsc.org/MaterialsA

Introduction

With the depletion of natural sources of energy and the use of fossil fuels having a negative impact on the environment, the demands for clean and sustainable energy have continued to increase. To fulfill these energy requirements, new technologies for energy storage and generation have been developed. As one of the most promising electrochemical energy storage device, rechargeable metal-air batteries have received much attention due to their many advantages. For instance, lithium-air and zinc-air batteries have extremely high practical energy densities of 1700 and 350 W h kg⁻¹, respectively, and are lightweight and cost effective as they operate on environmentally abundant oxygen from the air.¹⁻³ These advantages of metal-air batteries are highly suitable for implementation in electrical vehicle (EV) and hybrid electrical vehicle (HEV) applications to extend the driving range and replace currently used lithium ion batteries,

which provide insufficient storage capacity and require expensive intercalating materials.^{1,4,5} However, metal-air batteries face a set of challenges such as poor rate capability and cycle life.^{6,7} These technological hurdles mainly stem from inherently sluggish kinetics of the oxygen reduction reaction (ORR) and oxygen evolution reaction (OER), which are the two vital reactions that govern the discharge and charge, respectively, of a metal-air battery.⁸⁻¹⁰ In attempts to improve the kinetics of ORR and OER characteristics, carbon-supported electrocatalysts such as Pt, Pd, and its alloys have been used to increase the rate of the reactions.^{3,11-14} However, cost considerations of precious metal based catalysts and their poor electrochemical stability over long periods of operation have impeded their commercialization.^{15,16} In order to replace these expensive and unstable catalysts, numerous non-precious metal catalysts such as Fe-based materials and metal-free carbon-based catalysts such as nitrogen doped graphene have been developed in recent years.¹⁷⁻²⁰ Amongst these non-precious catalysts are transition metal-based oxide materials in the form of spinel and perovskite structures which have long been known to be electrocatalytically active.²¹⁻²³

One of the well-known spinel electrocatalysts is Co₃O₄ and it has been studied for decades as a highly efficient and

Department of Chemical Engineering, Waterloo Institute for Nanotechnology, Waterloo Institute for Sustainable Energy, University of Waterloo, Waterloo, ON, Canada N2L 3G1. E-mail: zhwchen@uwaterloo.ca; Fax: +1-519-746-4979; Tel: +1-519-888-4567 ext. 38664

† Electronic supplementary information (ESI) available: XPS spectra of NiCo₂O₄ and NiCo₂O₄-G. See DOI: 10.1039/c3ta01402a

corrosion-stable ORR and OER catalyst in alkaline media.^{24–27} To improve the electrochemical activity of Co_3O_4 electrocatalysts, researchers have incorporated Ni atoms into the spinel structure to form NiCo_2O_4 , which enhanced electrical conductivity of the metal oxide and increased the number of catalytically active sites.^{28,29} In addition, nanostructured NiCo_2O_4 , specifically nanowires, have been studied extensively to investigate the morphological effect on its electrochemical activity.^{28–32} However, to the best of our knowledge, there has not been any report on 2-dimensional mesoporous NiCo_2O_4 nanoplatelets as an electrocatalyst. Furthermore, there is no report on the combination of spinel NiCo_2O_4 nanostructures with carbon-based materials to improve the electrochemical properties of the metal oxide electrocatalyst. Graphene, with its intriguing properties such as large surface area, high electrical conductivity, and thermal and chemical stability,^{33–36} has been reported as an excellent support material as well as an active and stable electrocatalyst.^{37–39} For instance, extensive studies of graphene sheets have been reported as a support material for precious metal catalysts such as Pt, which demonstrated excellent electrochemical activity and stability.^{40,41} Also, graphene sheets as a metal-free catalyst have been shown to demonstrate an excellent performance in a hybrid electrolyte lithium–air battery.⁴² We speculate that by combining a transition metal oxide catalyst with a carbon-based support *via* a one-pot synthesis method as opposed to simple physical mixing will lead to a strong hybrid effect with catalytic contributions from both of their unique properties.

Therefore, we report a novel hybrid material composed of mesoporous NiCo_2O_4 nanoplatelets and graphene (NiCo_2O_4 -G) as an active bi-functional electrocatalyst for both ORR and OER. This hybrid material is synthesized *via* a one-pot method where the precursors of the metal-oxide (Ni and Co) and graphene sheets are mixed into a single reaction to produce the final material. The one-pot synthesis utilizes facile methods based on the precipitation reaction and hydrothermal process, which are very simple, cost effective, and highly efficient for producing large quantities of material. The evaluation of electrochemical activities of the hybrid towards ORR and OER is conducted by employing half-cell testing. We investigate the hybrid effect of combining NiCo_2O_4 nanoplatelets with graphene sheets by comparing its performance to that of NiCo_2O_4 itself without graphene sheets. The importance of PVP on the electrocatalytic activity is investigated by comparing the performance of NiCo_2O_4 -G to that of a hybrid created without the addition of PVP during synthesis—a capping agent that is responsible for controlling the morphology of NiCo_2O_4 nanostructures. We also demonstrate the advantages of incorporating an Ni atom into the spinel crystal structure by comparing the electrocatalytic activities of the hybrid with those of Co_3O_4 -G.

Experimental methods

Graphene oxide (GO) synthesis

GO is synthesized from natural graphite flakes by the modified Hummers' method.⁴³ In a typical GO preparation, 2 g of

graphite powder (Alfa Aesar) is stirred in 46 mL of concentrated sulphuric acid (Fisher Scientific) for 10 hours. The mixture is put into an ice bath and 1 g of sodium nitrate (Aldrich) is added followed by the addition of 6 g of potassium permanganate (EMD) under stirring. The mixture is removed from the ice bath and stirred for 1 hour. Then 92 mL of distilled de-ionized (DDI) water is added drop-wise and stirred for another 30 minutes followed by the addition of 280 mL of warm DDI water (40 °C) and 40 mL of 30% H_2O_2 (Fisher Scientific). The mixture is filtered and washed with 3 L of 5% HCl solution, and then centrifuged five times at 4000 rpm for 10 min. The product is collected and dried at room temperature.

One-pot synthesis of a mesoporous NiCo_2O_4 nanoplatelet and graphene hybrid

The one-pot synthesis of a mesoporous NiCo_2O_4 -G hybrid is carried out by concurrent precipitation and hydrothermal reactions. In a typical synthesis, 1.65 g of polyvinylpyrrolidone (PVP) with a molecular weight of 24 000 is dissolved in a 10 mL mixture of double deionized (DDI) water and ethanol with a 1 : 1 volume ratio. Then, 0.419 g and 0.833 g of $\text{Ni}(\text{NO}_3)_2 \cdot 6\text{H}_2\text{O}$ and $\text{Co}(\text{NO}_3)_2 \cdot 6\text{H}_2\text{O}$, respectively, were dissolved in the PVP solution, and magnetically stirred for 30 minutes with the mixture bubbled with N_2 . Next, 0.213 mL of a 1.0 M NaOH aqueous solution was added dropwise at a rate of 0.56 mL min^{-1} to induce a precipitation reaction, followed by the addition of 100 mg of GO. Then, 6 mL of NH_4OH is added and stirred vigorously for 30 minutes. The suspension was then transferred to a Teflon-lined autoclave, sealed and then heated at 120 °C for 6 hours. The autoclave is naturally cooled to room temperature, then the precipitate is collected and centrifuged three times with DDI and another 3 times with acetone at 5000 rpm to remove any impurities and excess PVP. The obtained black slurry is freeze dried for 24 hours, turning into a fine powder, which is calcined in air at 300 °C for 3 hours to obtain the final product.

Material characterization

Scanning electron microscopy (SEM) (LEO FESEM 1530) and transmission electron microscopy (TEM) (Philips CM300) were utilized to observe the morphology and surface structure. High-resolution TEM (HR-TEM), fast Fourier transformation (FFT) patterns, and selected area electron diffraction (SAED) patterns were used to study the crystallinity of the spinel nanoplatelets in the NiCo_2O_4 -G hybrid. The nitrogen adsorption–desorption isotherm was obtained by Brunauer–Emmett–Teller (BET) using a Micromeritics ASAP 2020 surface area and porosity analyzer. The pore size distributions were evaluated by using the Barrett–Joyner–Halenda (BJH) model. X-ray diffraction (XRD) (Bruker AXS D8 Advance) was used to verify the spinel crystal structure of nanoplatelets in the NiCo_2O_4 -G hybrid, and X-ray photoelectron spectroscopy (XPS) (Thermal Scientific K-Alpha XPS spectrometer) was conducted to identify the atomic composition of the hybrid and to elucidate the electronic configurations of Ni and Co cations in the spinel structure.

Three-electrode half-cell test

The electrochemical activities of the materials developed in the present work were tested in an aqueous electrolyte (0.1 M KOH) using a standard three-electrode electrochemical cell *via* rotating disk electrode (RDE) voltammetry for ORR and cyclic voltammetry (CV) for OER. The setup for RDE and CV consists of a potentiostat (Pine Instrument Co., AFCBP-1) and a rotation speed controller (Pine Instrument Co., AFMSRCE). All electrochemical testing was performed at room temperature using a Saturated Calomel Electrode (SCE) as a reference electrode. A platinum wire was used as the counter electrode. A glassy carbon electrode (5 mm OD) coated with 20 μL of 4 mg mL^{-1} suspension made by mixing $\text{NiCo}_2\text{O}_4\text{-G}$ and a solution of 0.5 wt% Nafion in ethanol was used as the working electrode. The same preparation of the working electrode was used for all other comparison materials. ORR curves were recorded from -1.0 to 0.2 V at a scan rate of 10 mV s^{-1} with an O_2 -saturated electrolyte under various electrode rotation speeds (100, 400, 900, and 1600 rpm). The ORR polarization curves were background corrected by subtracting the currents obtained under the same testing conditions in an N_2 -saturated electrolyte. The OER curves were

recorded from 0 to 1.0 V at a scan rate of 50 mV s^{-1} with a N_2 -saturated electrolyte with a rotation speed of 900 rpm in order to spin off the oxygen evolved during voltammetry testing.

Results and discussion

The structure and surface morphology of the mesoporous $\text{NiCo}_2\text{O}_4\text{-G}$ hybrid formed by a one-pot synthesis method are characterized using SEM. During synthesis, PVP plays two important roles in controlling the final morphology of the hybrid. First, PVP is well-known to coordinate to the surface of metal ions such as cobalt ions through $-\text{N}$ and/or $\text{C}=\text{O}$ groups of the pyrrolidone ring.⁴⁴ Hence, PVP acts as a capping agent in a mix of H_2O and ethanol solution by selectively adsorbing onto specific crystallographic planes to provide spatial confinements for anisotropic growth of NiCo_2O_4 into 2-dimensional nanoplatelets^{45,46} (Fig. 1a). Second, the surface adsorbed PVP decomposes upon the calcination process in air at 300°C for 3 h to leave behind meso-sized pores in the nanoplatelets (Fig. 1b). A detailed inspection of the nanoplatelets using TEM clearly shows well-distributed mesopores in the nanoplatelets with a

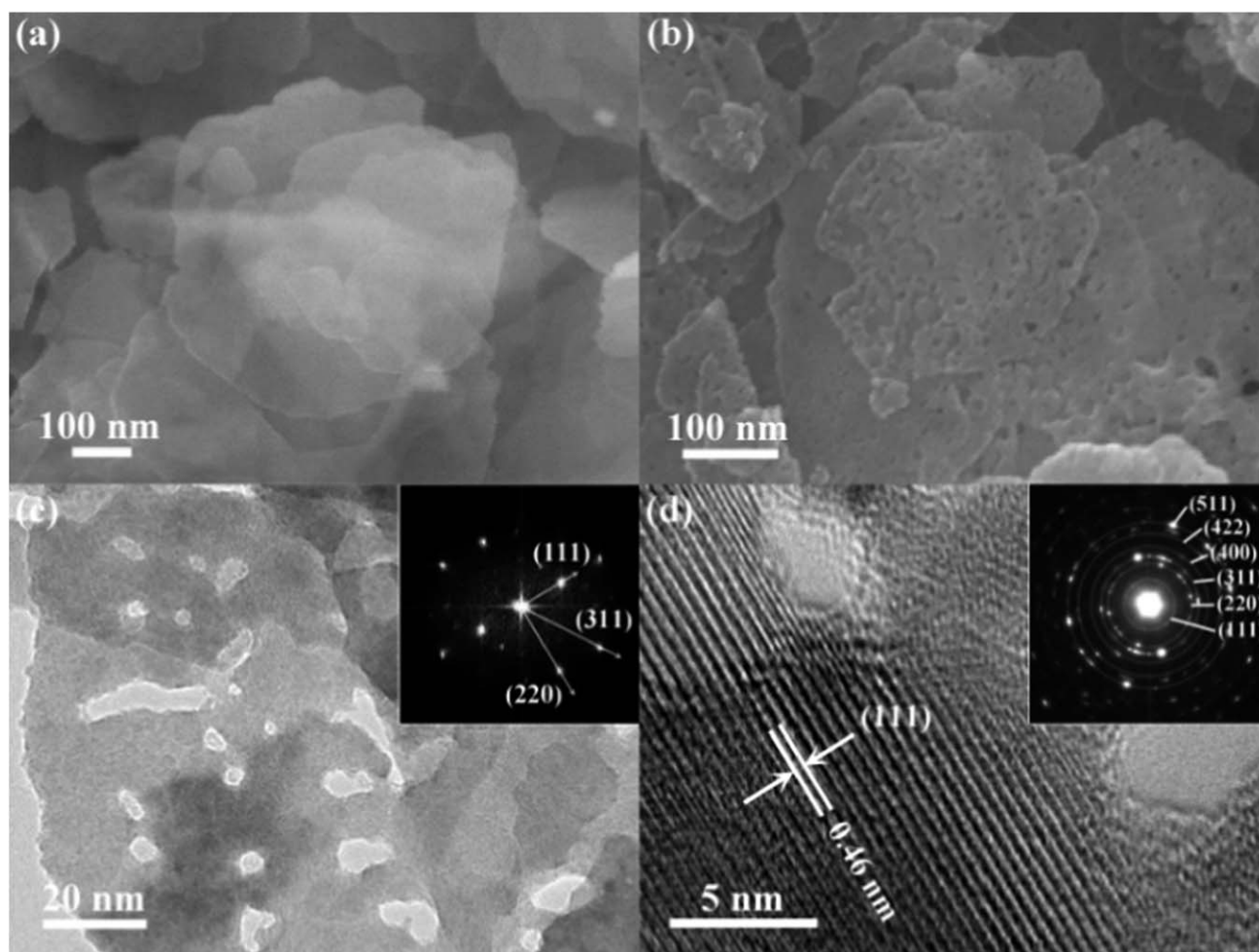


Fig. 1 (a) SEM image of uncalcined $\text{NiCo}_2\text{O}_4\text{-G}$ prior to the formation of mesopores on the nanoplatelets. (b) SEM image of calcined $\text{NiCo}_2\text{O}_4\text{-G}$ with mesopores on the nanoplatelets. (c) TEM image of $\text{NiCo}_2\text{O}_4\text{-G}$ uniformly distributed mesopores. Inset, the FFT pattern of cubic spinel NiCo_2O_4 nanoplatelets in the hybrid. (d) HR-TEM image of the (111) crystal plane of spinel NiCo_2O_4 nanoplatelets. Inset, the SAED pattern of spinel NiCo_2O_4 nanoplatelets in the hybrid.

variety of sizes and shapes (Fig. 1c). This unique porous structure is likely to create more active sites with increased surface area and facilitates in the transport of reactant species during electrocatalysis. NiCo_2O_4 nanoplatelets exhibit a highly crystalline structure as confirmed by distinct diffraction dots observed in the FFT pattern (Fig. 1c, inset). Further analyzing the FFT pattern has revealed characteristic crystallographic orientations of (111), (220), and (311) for the spinel NiCo_2O_4 . In addition, calculation of the d -spacing using the fringes observed in the HR-TEM image of the nanoplatelets has resulted in 0.46 nm (Fig. 1d), which very closely match with the theoretical d -spacing for the (111) orientation of a cubic spinel of NiCo_2O_4 (0.46 nm) [JCPDS: 20-0781]. The high crystallinity of the nanoplatelets has also been confirmed by SAED, which shows a clear diffraction pattern for various crystallographic planes of the spinel (Fig. 1d, inset).

The BET characterization has been carried out to confirm the mesoporous nature of $\text{NiCo}_2\text{O}_4\text{-G}$. The nitrogen adsorption-desorption curves demonstrate a Type IV isotherm, and a distinct hysteresis loop in the P/P_0 range of 0.6 to 1.0 (Fig. 2a), which are strong indications of capillary condensation and multilayer adsorption, hence the presence of mesopores. The BET specific surface area is found to be $77 \text{ m}^2 \text{ g}^{-1}$, higher than that of the previously reported graphene-nickel cobaltite nanocomposite.⁴⁷

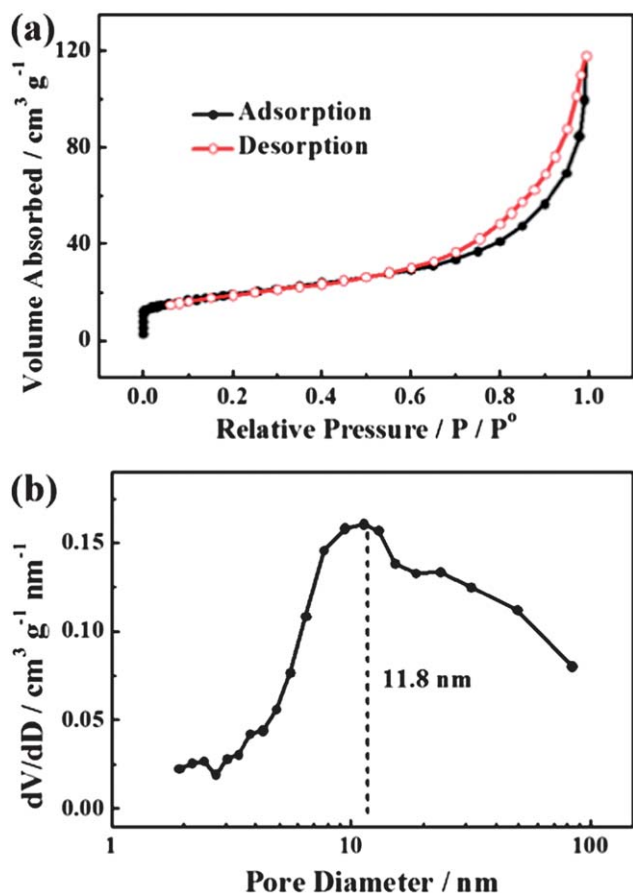


Fig. 2 (a) Nitrogen adsorption-desorption isotherm loop and pore size distribution curve calculated by the BJH model of $\text{NiCo}_2\text{O}_4\text{-G}$.

The higher specific surface area enhances the exposure of active sites available for reaction on the surface. The outstanding electrocatalytic activity of $\text{NiCo}_2\text{O}_4\text{-G}$ is most likely ascribed to this increased number of active sites as both ORR and OER are surface reactions. The pore size distribution calculated by the BJH model shows a predominant peak in the meso-scale of 5 to 15 nm with an average pore diameter of 11.8 nm (Fig. 2b), consistent with pore sizes observed by HR-TEM analysis (Fig. 1c). The broad pore distribution in the range of 15 to 100 nm is probably due to the interlayer spacings formed between nanoplatelets and graphene sheets. Hence, it can be concluded from the isotherm and the pore size distribution that $\text{NiCo}_2\text{O}_4\text{-G}$ consists of mesopores which enhance the electrocatalytic activity by increasing the surface exposure of the active sites.

The crystal structure of $\text{NiCo}_2\text{O}_4\text{-G}$ is further investigated by XRD (Fig. 3), and the characteristic peaks are well indexed to those of spinel NiCo_2O_4 [JCPDS: 20-0781]. The XRD pattern of $\text{NiCo}_2\text{O}_4\text{-G}$ compared to that of $\text{Co}_3\text{O}_4\text{-G}$, which is synthesized using the same procedure but the Co metal precursor replacing that of Ni, also demonstrates spinel crystallinity. However, the peaks are relatively broad in the case of $\text{NiCo}_2\text{O}_4\text{-G}$, which is indicative of smaller crystallites formed due to the change in the structure with the addition of Ni atoms into the spinels of Co_3O_4 . The d -spacing of each crystal orientation observed in the XRD pattern is calculated based on the diffraction angle using Bragg's law, and they match closely with those calculated with the SAED pattern from the TEM characterization (Table 1), signifying a successful synthesis of NiCo_2O_4 spinels. Additionally, using the d -spacing of the (400) plane, the lattice parameter (a_0) of the cubic spinel structure is determined to be 0.803 nm. This is slightly larger than 0.801 nm of $\text{Co}_3\text{O}_4\text{-G}$, which is consistent with the literature where the incorporation of Ni into the Co_3O_4 spinel is known to expand the elementary spinel lattice.^{48,49}

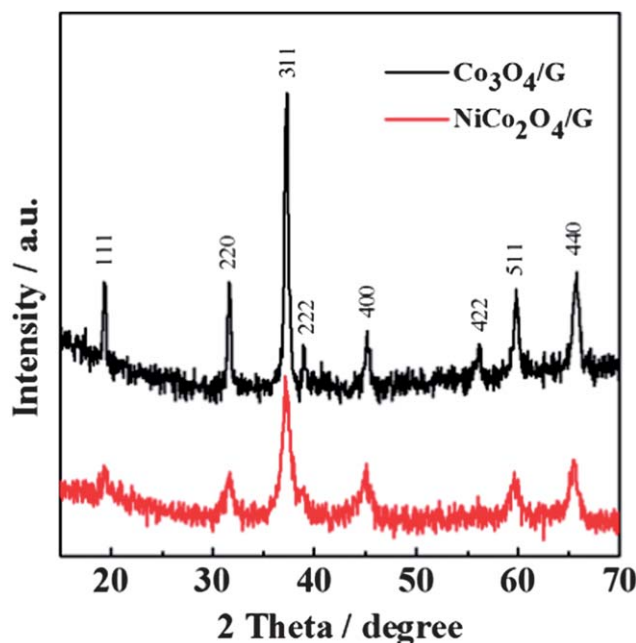


Fig. 3 XRD patterns of the spinel crystal structure in $\text{NiCo}_2\text{O}_4\text{-G}$ and $\text{Co}_3\text{O}_4\text{-G}$ hybrids.

Table 1 Calculated values of *d*-spacing for each crystal orientation observed in the SAED pattern obtained from TEM and diffraction angles obtained from XRD of NiCo₂O₄-G

Crystal orientation	TEM		XRD	
	Diffraction radius (nm ⁻¹)	<i>d</i> -Spacing (nm)	2 Theta (degree)	<i>d</i> -Spacing (nm)
440	7.00	0.143	65.50	0.142
511	6.91	0.146	59.60	0.155
422	6.02	0.166	56.22	0.163
400	4.90	0.204	45.10	0.201
311	4.06	0.246	37.21	0.241
220	3.53	0.283	31.70	0.282
111	2.18	0.459	19.34	0.458

The surface elemental compositions and electronic configurations of the atoms in the hybrid are investigated by employing XPS. As expected, a full survey of NiCo₂O₄-G revealed peaks corresponding to the existence of Ni 2p, Co 2p, O 1s, and C 1s (Fig. 4a). The de-convolution of the Ni 2p peaks shows the atoms in 2P_{1/2} and 2P_{3/2} electronic configurations at 872.78 eV and 855.38 eV, respectively (Fig. 4b). Similarly, the de-convoluted Co 2p shows the electronic configuration of Co atoms in 2P_{1/2} and 2P_{3/2} states at 795.28 eV and 779.98 eV, respectively (Fig. 4c). The binding energies of these peaks are consistent with the literature and signify the formation of cubic spinel NiCo₂O₄. The O 1s shows a large M-O-M peak at 529.48 eV which is indicative of most of the oxygen in the lattice, with the other two peaks C=O and O-C=O bonds, at 532.83 and

531.15 eV, respectively, which correspond to oxygen groups of the graphene sheets most likely due to an incomplete reduction and also due to the moisture adsorbed onto the graphene sheets under ambient conditions (Fig. 4d). The comparison of XPS spectra of NiCo₂O₄ and NiCo₂O₄-G for the elements Ni, Co, and C has revealed no shift in the binding energy of the peaks after the hybridization of the metal oxide and graphene sheets (Fig. S1a-c[†]). However, a positive shift in the binding energy for the O 1s peak is observed for NiCo₂O₄-G compared to that of NiCo₂O₄ (Fig. S1d[†]). This is an indication that the hybridization is probably occurring through the oxygen species of GO, which has most likely reacted with the metal precursors at the time of the one-pot synthesis.

The electrochemical characterization of NiCo₂O₄-G is conducted by performing three-electrode half-cell testing in 0.1 M KOH. The catalysis of ORR using the NiCo₂O₄-G hybrid as the electrocatalyst is studied by RDE voltammetry. As expected, the polarization curves of the hybrid obtained at various rotation speeds show a well-defined drop in the current density for oxygen reduction in the mixed kinetic- and diffusion-limiting region followed by a plateau at a stable current density in the diffusion-limited region (Fig. 5a). Using these polarization curves, several potential points are selected between 0.65 and 0.90 V (*vs.* SCE) to determine the Koutecky-Levich slope, which is used to calculate the number of electrons transferred, *n*, during the ORR (Fig. 4a, inset). The analysis of the plot has resulted in *n* = 3.9 confirming that the ORR catalyzed by the hybrid occurs in a highly desirable pseudo four-electron reduction pathway (O₂ + 2H₂O + 4e⁻ → 4OH⁻). This excellent electrochemical activity of the hybrid towards ORR is attributed to the incorporation of Ni atoms into the spinel structure as observed by a much enhanced ORR polarization curve of NiCo₂O₄-G at a rotation rate of 900 rpm compared to that of Co₃O₄-G with the same structure and surface morphology (Fig. 5b). In terms of the onset potential, the hybrid exhibits a much higher value of -0.12 V compared to -3.00 V of Co₃O₄-G. Furthermore, the half-wave potential (HWP) of the hybrid demonstrated a much higher value of -0.27 V compared to -0.41 V of Co₃O₄-G. These enhancements observed in the onset potential and HWP are strong indications of highly efficient active sites of NiCo₂O₄-G towards ORR. In addition, a significant increase in the stable current density obtained in the diffusion-limited region is indicative of increased accessibility of O₂ onto the active sites for enhanced ORR activity, which could be attributed to the smaller crystallite size of the NiCo₂O₄-G hybrid observed from the broad peaks of the XRD pattern.

This excellent ORR activity of the hybrid is ascribed to the creation of highly efficient active sites created by Ni cations in the spinel lattice. Also, previous literature has shown that the insertion of Ni into the octahedral sites of the spinel increases the electrical conductivity, which is highly desirable for fast charge transfer during ORR.²⁹ Even though some spinel metal oxides are known to exhibit high electrocatalytic activities,³⁰ metal oxides have relatively lower electrical conductivity than carbon-based materials such as graphene sheets. This may prevent efficient utilization of active sites of the metal oxide that

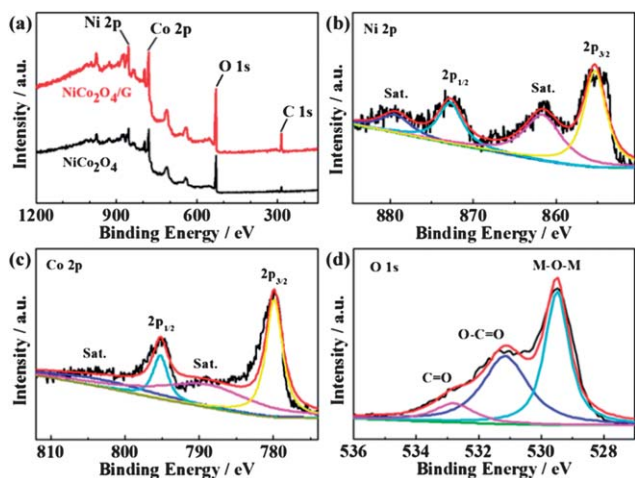


Fig. 4 (a) Full XPS spectra of the NiCo₂O₄-G hybrid and graphene-free NiCo₂O₄. (b) High-resolution Ni 2p XPS spectra of NiCo₂O₄-G. (c) High-resolution Co 2p XPS spectra of NiCo₂O₄-G. (Note for (b) and (c): the black line is the original signal, and the red curve is the result of the curve fit. Yellow and cyan peaks correspond to 2p_{3/2} and 2p_{1/2} species, respectively, and pink and blue peaks correspond to the associated satellite species, after de-convolution.) (d) High-resolution O 1s XPS spectra of NiCo₂O₄-G. (The black line is the original signal, and the red curve is the result of the curve fit. Cyan, blue, and pink peaks correspond to lattice oxygen. Yellow and cyan peaks correspond to 2p_{3/2} and 2p_{1/2} species, respectively, and pink and navy peaks corresponds to the associated satellite species, after de-convolution.)

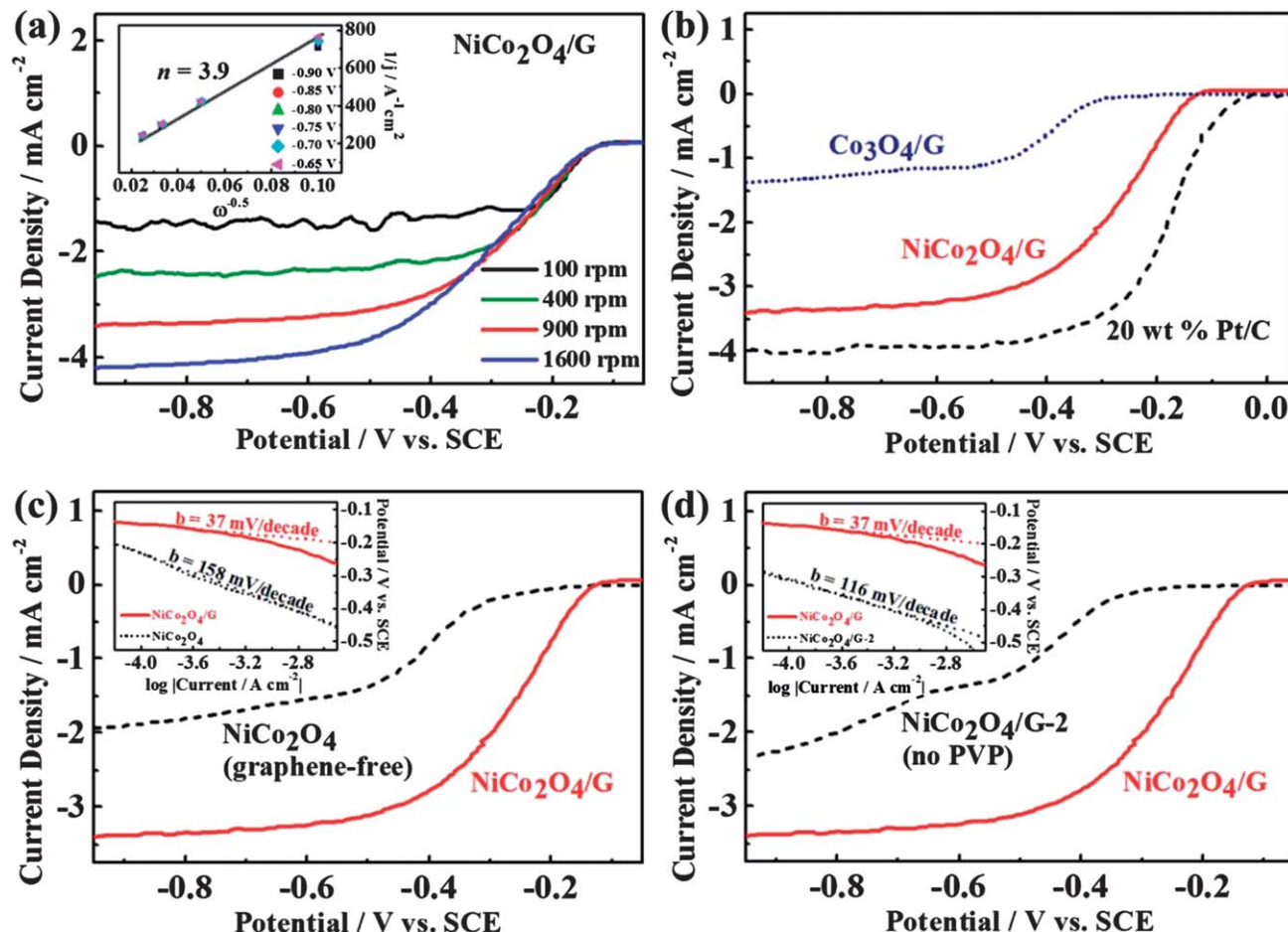


Fig. 5 (a) ORR polarization curves of NiCo₂O₄-G obtained by RDE voltammetry in O₂-saturated 0.1 M KOH at various rotation rates. Inset, the Koutecký–Levich plot of NiCo₂O₄-G at potentials -0.65, -0.70, -0.75, -0.80, -0.85, and -0.90 V (vs. SCE). (b) ORR polarization curves of NiCo₂O₄-G, Co₃O₄-G, and 20 wt% Pt/C at a rotation rate of 900 rpm. ORR polarization curves and Tafel plots (inset) of (c) NiCo₂O₄ and NiCo₂O₄-G, and (d) NiCo₂O₄-G-2 and NiCo₂O₄-G at a rotation rate of 900 rpm.

are available for electrocatalytic activity. Hence, by combining NiCo₂O₄ with graphene sheets into a hybrid, a much enhanced ORR polarization curve is observed compared to that of graphene-free NiCo₂O₄ itself (Fig. 5c). Graphene-free NiCo₂O₄ is synthesized in the same way as the hybrid but without the addition of GO during the one-pot synthesis. The polarization curve of the hybrid clearly shows a significantly higher (more negative) limiting current density, which is an indication of an increased number of active sites for ORR. In the hybrid, graphene sheets most likely facilitate the distribution of the metal oxide nanoplatelets to prevent agglomeration of particles, thereby increasing the number of active sites. Furthermore, the enhancement in the onset potential of the hybrid may be an indication that the graphene sheets themselves are catalytically active, which have been reported in the literature as an ORR-active catalyst,^{42,51} since the ORR kinetics of NiCo₂O₄ should be the same in the case of both the hybrid and the metal oxide itself. The analysis of the Tafel plot has resulted in a much lower slope for the hybrid in the lower overpotential region compared to the metal oxide itself. This is indicative of enhanced ORR kinetics with the addition of graphene sheet, which is consistent with the previous observation (Fig. 5c, inset). The PVP effect

of the nanoplatelets is investigated by comparing the ORR polarization curve of the NiCo₂O₄-G hybrid with that of a hybrid synthesized by the same procedure as NiCo₂O₄-G but without the addition of PVP (NiCo₂O₄-G-2) (Fig. 5d). The observation of the ORR polarization curve of NiCo₂O₄-G-2 suggests that the oxygen reduction proceeds in a two-electron reduction pathway, which is highly undesirable due to an inefficient catalytic activity and the formation of peroxide species which may promote electrocatalyst degradation. The NiCo₂O₄-G hybrid exhibits increased (more negative) limiting current density in the diffusion-limited region most likely due to a higher surface area from the mesopores in the nanoplatelets, which would be absent in the case of NiCo₂O₄-G-2. In addition, improved onset potential and HWP are observed for NiCo₂O₄-G with a significantly lower Tafel slope compared to that of NiCo₂O₄-G-2 (116 mV per decade) (Fig. 5d, inset). These enhanced ORR characteristics are ascribed to more efficient active sites created with the addition of PVP during the synthesis of NiCo₂O₄-G.

The oxygen evolution activity of the NiCo₂O₄-G hybrid is investigated by analyzing CV curves obtained by half-cell testing. The CV curve of NiCo₂O₄-G shows the anodic peak at 0.49 V (and its corresponding cathodic peak at 0.28 V), which

corresponds to the transition of the redox couple Ni(III)/Ni(IV). This redox couple is known to be the cation in the octahedral site of the spinel that is responsible for the catalysis of OER.^{28,29} This anodic peak is followed by the onset of oxygen evolution and the dramatic increase in the current density due to the excellent OER activity of the hybrid. Peaks that correspond to the redox couple Ni(II)/Ni(III) and Co(II)/Co(III) are not visible in the CV curve because these cations located in the tetrahedral sites of the spinel are much more difficult to oxidize or reduce than those in the octahedral sites.^{49,52} In order to elucidate the effect of graphene in the hybrid, the OER activity of the hybrid is compared to that of NiCo₂O₄ itself (Fig. 6a). The onset potential of oxygen evolution is much lower for the hybrid (0.55 V) compared to that of graphene-free NiCo₂O₄ (0.62 V), indicative of much lower activation energy for OER with the addition of graphene sheets. Furthermore, the hybrid exhibits a much higher current density at 0.95 V of 35.4 mA cm⁻² compared to only 18.6 mA cm⁻² for the graphene-free NiCo₂O₄. This excellent OER activity of the hybrid is attributed to the high electrical conductivity provided by graphene sheets which facilitates charge transfer during the reaction at the surface of the metal oxide. The investigation of OER kinetics *via* the Tafel analysis in the low overpotential region has confirmed a much faster OER

activity indicated by a much lower slope of 161 mV per decade of the hybrid compared to 205 mV per decade of the metal-oxide itself (Fig. 6a, inset). In addition, the effect of adding PVP during the synthesis is highly beneficial for the OER activity of NiCo₂O₄-G as a significantly higher OER current density of 35.4 mA cm⁻² is observed at 0.95 V compared to that of only 21.4 mA cm⁻² for NiCo₂O₄-G-2 (Fig. 6b). The analysis of the Tafel plot of NiCo₂O₄-G-2 has resulted in an unusually high Tafel slope of 799 mV per decade, which is indicative of very slow OER kinetics (Fig. 6b, inset). The enhanced OER performance of NiCo₂O₄-G is again ascribed to more efficient active sites with much lower energy barrier created with the addition of PVP during the synthesis of NiCo₂O₄-G. Furthermore, to study the effect of the addition of Ni species into the spinel crystal structure, the OER activity of NiCo₂O₄-G is compared to that of Co₃O₄-G (Fig. 6c). Without the addition of Ni, Co₃O₄-G is observed to exhibit a much lower current density of 18.35 mA cm⁻² at 0.95 V compared to that of 36.4 mA cm⁻² for NiCo₂O₄-G. Similar to the ORR performance, this enhancement in OER activity is due to the Ni species in the octahedral sites of the spinel that create active sites for OER with much lower activation potential compared to that of the Co cation. The electrochemical durability of the hybrid is evaluated by

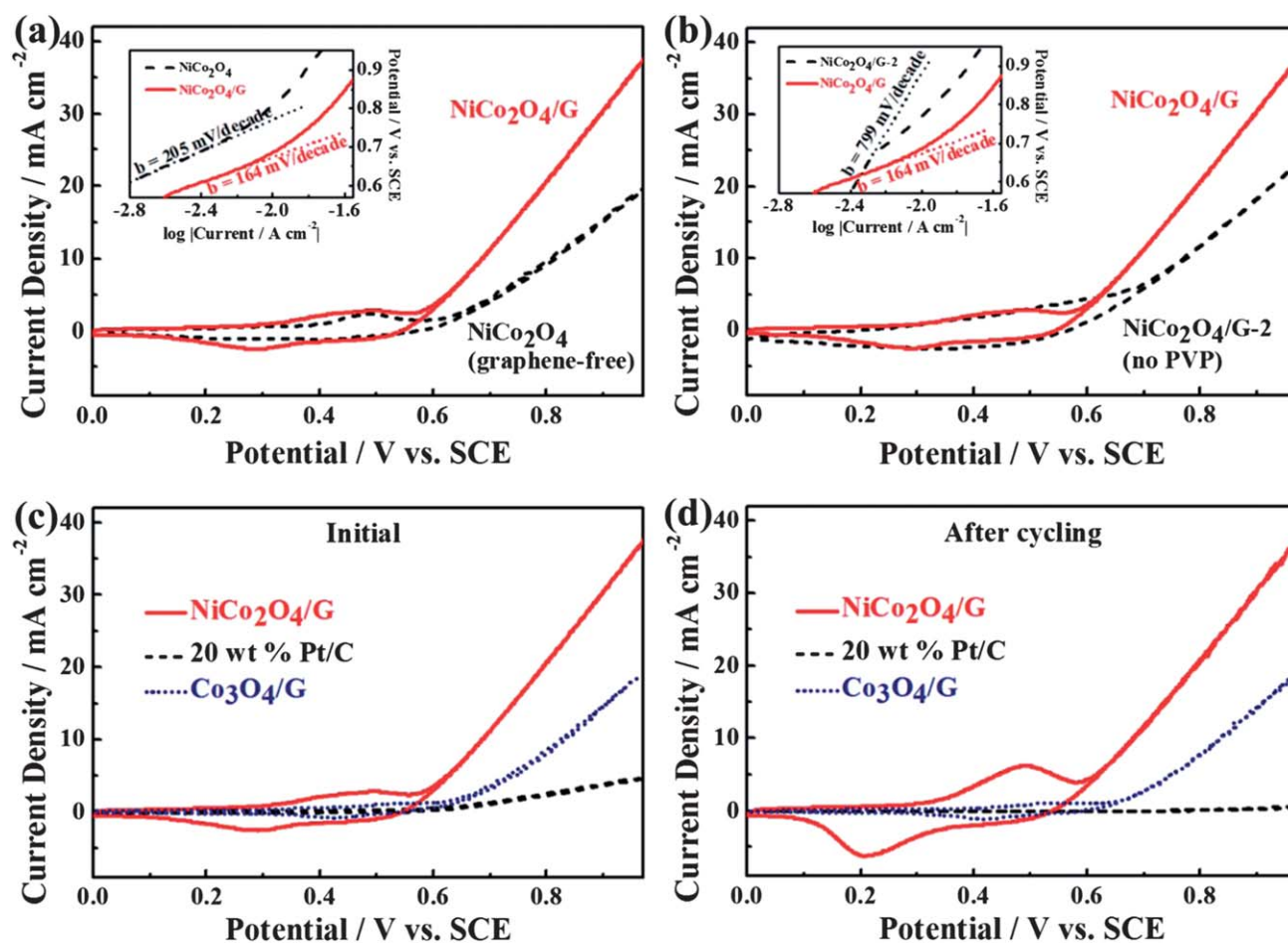


Fig. 6 OER CV curves and Tafel plots (inset) of (a) NiCo₂O₄ and NiCo₂O₄-G, and (b) NiCo₂O₄-G-2 and NiCo₂O₄-G obtained by N₂-saturated 0.1 M KOH at a rotation rate of 900 rpm. OER CV curves of NiCo₂O₄-G, Co₃O₄-G and 20 wt% Pt/C (c) initial cycle and (d) after 1000 CV cycles.

repeating the CV cycle 1000 times (Fig. 6d). After cycling, the current density retention at 0.95 V is 99.6% for the hybrid. The cobalt oxide hybrid has also exhibited a very stable OER durability with 98.6% current density retention, however, the commercial Pt/C has degraded very heavily, resulting in a very low current density retention of 8.0%. This excellent durability demonstrated by NiCo₂O₄-G attributed to the graphene sheets in the hybrid acting as a support for the electrocatalyst to provide fast charge transfer and prevent agglomeration of the nanoplatelets.

Conclusions

In summary, we have synthesized a mesoporous NiCo₂O₄ nanoplatelet-graphene hybrid as a highly active bi-functional catalyst for oxygen reduction and oxygen evolution reactions by a one-pot precipitation reaction and hydrothermal process. The hybrid effect of NiCo₂O₄-G on ORR and OER activities confirmed by RDE and CV measurements, respectively, is attributed to much faster charge transfer facilitated by graphene sheets as a support material. Also, the addition of PVP during synthesis is highly beneficial for enhanced ORR and OER activities most likely due to the formation of highly efficient active sites of the nanoplatelets. Finally, the incorporation of Ni atoms into the spinel lattice is found to significantly improve both ORR and OER performances of Co₃O₄-G. This is ascribed to the increased electrical conductivity and the creation of new active sites by Ni incorporation into the octahedral sites of the spinel crystal structure.

Acknowledgements

This research was supported by the Natural Sciences and Engineering Research Council of Canada (NSERC) through grants to Dr Zhongwei Chen, the University of Waterloo, and the Waterloo Institute for Nanotechnology.

Notes and references

- G. Girishkumar, B. McCloskey, A. C. Luntz, S. Swanson and W. Wilcke, *J. Phys. Chem. Lett.*, 2010, **1**, 2193–2203.
- Z. Chen, A. Yu, D. Higgins, H. Li, H. Wang and Z. Chen, *Nano Lett.*, 2012, **12**, 1946–1952.
- J.-S. Lee, S. Tai Kim, R. Cao, N.-S. Choi, M. Liu, K. T. Lee and J. Cho, *Adv. Energy Mater.*, 2011, **1**, 34–50.
- S. M. Lukic, C. Jian, R. C. Bansal, F. Rodriguez and A. Emadi, *IEEE Transactions on Industrial Electronics*, 2008, **55**, 2258–2267.
- B. Scrosati and J. Garche, *J. Power Sources*, 2010, **195**, 2419–2430.
- Y.-C. Lu, H. A. Gasteiger and Y. Shao-Horn, *Electrochem. Solid-State Lett.*, 2011, **14**, A70–A74.
- Y.-C. Lu, D. G. Kwabi, K. P. C. Yao, J. R. Harding, J. Zhou, L. Zuin and Y. Shao-Horn, *Energy Environ. Sci.*, 2011, **4**, 2999–3007.
- J.-S. Lee, G. S. Park, H. I. Lee, S. T. Kim, R. Cao, M. Liu and J. Cho, *Nano Lett.*, 2011, **11**, 5362–5366.
- V. Neburchilov, H. Wang, J. J. Martin and W. Qu, *J. Power Sources*, 2010, **195**, 1271–1291.
- Z. W. Chen, D. Higgins, A. P. Yu, L. Zhang and J. J. Zhang, *Energy Environ. Sci.*, 2011, **4**, 3167–3192.
- S. Guo, S. Dong and E. Wang, *ACS Nano*, 2009, **4**, 547–555.
- A. Kongkanand, S. Kuwabata, G. Girishkumar and P. Kamat, *Langmuir*, 2006, **22**, 2392–2396.
- Y. H. Bing, H. S. Liu, L. Zhang, D. Ghosh and J. J. Zhang, *Chem. Soc. Rev.*, 2010, **39**, 2184–2202.
- D. C. Higgins, D. Meza and Z. Chen, *J. Phys. Chem. C*, 2010, **114**, 21982–21988.
- K. Gong, F. Du, Z. Xia, M. Durstock and L. Dai, *Science*, 2009, **323**, 760–764.
- Y. Liang, H. Wang, J. Zhou, Y. Li, J. Wang, T. Regier and H. Dai, *J. Am. Chem. Soc.*, 2012, **134**, 3517–3523.
- J.-Y. Choi, D. Higgins and Z. Chen, *J. Electrochem. Soc.*, 2012, **159**, B87–B90.
- J. Wu, W. Li, D. Higgins and Z. Chen, *J. Phys. Chem. C*, 2011, **115**, 18856–18862.
- D. Higgins, Z. Chen and Z. Chen, *Electrochim. Acta*, 2011, **56**, 1570–1575.
- Z. Chen, J.-Y. Choi, H. Wang, H. Li and Z. Chen, *J. Power Sources*, 2011, **196**, 3673–3677.
- A. C. Tavares, M. A. M. Cartaxo, M. I. da Silva Pereira and F. M. Costa, *J. Electroanal. Chem.*, 1999, **464**, 187–197.
- I. Nikolov, R. Darkaoui, E. Zhecheva, R. Stoyanova, N. Dimitrov and T. Vitanov, *J. Electroanal. Chem.*, 1997, **429**, 157–168.
- N. Fradette and B. Marsan, *J. Electrochem. Soc.*, 1998, **145**, 2320–2327.
- V. Rashkova, S. Kitova, I. Konstantinov and T. Vitanov, *Electrochim. Acta*, 2002, **47**, 1555–1560.
- S. P. Singh, S. Samuel, S. K. Tiwari and R. N. Singh, *Int. J. Hydrogen Energy*, 1996, **21**, 171–178.
- L. Jörissen, *J. Power Sources*, 2006, **155**, 23–32.
- S. M. Jasem and A. C. C. Tseung, *J. Electrochem. Soc.*, 1979, **126**, 1353–1360.
- Y. Li, P. Hasin and Y. Wu, *Adv. Mater.*, 2010, **22**, 1926–1929.
- B. Lu, D. Cao, P. Wang, G. Wang and Y. Gao, *Int. J. Hydrogen Energy*, 2011, **36**, 72–78.
- R. R. Salunkhe, K. Jang, H. Yu, S. Yu, T. Ganesh, S.-H. Han and H. Ahn, *J. Alloys Compd.*, 2011, **509**, 6677–6682.
- H. Wang, Q. Gao and L. Jiang, *Small*, 2011, **7**, 2454–2459.
- C. Yuan, J. Li, L. Hou, L. Yang, L. Shen and X. Zhang, *J. Mater. Chem.*, 2012, **22**, 16084–16090.
- A. K. Geim and K. S. Novoselov, *Nat. Mater.*, 2007, **6**, 183–191.
- S. Yang, X. Feng, X. Wang and K. Müllen, *Angew. Chem., Int. Ed.*, 2011, **50**, 5339–5343.
- H. Wang, Y. Yang, Y. Liang, J. T. Robinson, Y. Li, A. Jackson, Y. Cui and H. Dai, *Nano Lett.*, 2011, **11**, 2644–2647.
- G. Yu, L. Hu, M. Vosgueritchian, H. Wang, X. Xie, J. R. McDonough, X. Cui, Y. Cui and Z. Bao, *Nano Lett.*, 2011, **11**, 2905–2911.
- L. Qu, Y. Liu, J.-B. Baek and L. Dai, *ACS Nano*, 2010, **4**, 1321–1326.
- K. R. Lee, K. U. Lee, J. W. Lee, B. T. Ahn and S. I. Woo, *Electrochem. Commun.*, 2010, **12**, 1052–1055.

- 39 D. Geng, Y. Chen, Y. Chen, Y. Li, R. Li, X. Sun, S. Ye and S. Knights, *Energy Environ. Sci.*, 2011, **4**, 760–764.
- 40 M. H. Seo, S. M. Choi, H. J. Kim and W. B. Kim, *Electrochem. Commun.*, 2011, **13**, 182–185.
- 41 B. Seger and P. V. Kamat, *J. Phys. Chem. C*, 2009, **113**, 7990–7995.
- 42 E. Yoo and H. Zhou, *ACS Nano*, 2011, **5**, 3020–3026.
- 43 W. S. Hummers and R. E. Offeman, *J. Am. Chem. Soc.*, 1958, **80**, 1339.
- 44 X. Wang, X. L. Wu, Y. G. Guo, Y. T. Zhong, X. Q. Cao, Y. Ma and J. N. Yao, *Adv. Funct. Mater.*, 2010, **20**, 1680–1686.
- 45 Y. Sun and Y. Xia, *Science*, 2002, **298**, 2176–2179.
- 46 Y. Sui, W. Fu, H. Yang, Y. Zeng, Y. Zhang, Q. Zhao, Y. Li, X. Zhou, Y. Leng, M. Li and G. Zou, *Cryst. Growth Des.*, 2009, **10**, 99–108.
- 47 H. Wang, C. B. Holt, Z. Li, X. Tan, B. Amirkhiz, Z. Xu, B. Olsen, T. Stephenson and D. Mitlin, *Nano Res.*, 2012, **5**, 605–617.
- 48 I. Nikolov, R. Darkaoui, E. Zhecheva, R. Stoyanova, N. Dimitrov and T. Vitanov, *J. Electroanal. Chem.*, 1997, **429**, 157–168.
- 49 E. B. Castro and C. A. Gervasi, *Int. J. Hydrogen Energy*, 2000, **25**, 1163–1170.
- 50 M. Hamdani, R. N. Singh and P. Chartier, *Int. J. Electrochem. Sci.*, 2010, **5**, 556–577.
- 51 L. Tang, Y. Wang, Y. Li, H. Feng, J. Lu and J. Li, *Adv. Funct. Mater.*, 2009, **19**, 2782–2789.
- 52 I. D. Belova, Y. E. Roginskaya, R. R. Shifrina, S. G. Gagarin, Y. V. Plekhanov and Y. N. Venetsev, *Solid State Commun.*, 1983, **47**, 577–584.